Jia *et al. Energy Mater.* **2025**, *5*, 500073
DOI: 10.20517/energymater.2024.291

Energy Materials

Article

Open Access

Tailoring hard carbon interfaces in carbonate-based electrolytes for sodium-ion hybrid capacitors

Ziyang Jia[1], Shunkang Hou[1], Xi Chen[1], Lili Liu[1,*], Xinhai Yuan[1,*], Lijun Fu[1], Yuhui Chen[1], Yuping Wu[1,2,*]

[1]School of Energy Science and Engineering, Nanjing Tech University, Nanjing 211816, Jiangsu, China.
[2]Confucius Energy Storage Lab, School of Energy and Environment & Z Energy Storage Center, Southeast University, Nanjing 211189, Jiangsu, China.

***Correspondence to:** Prof./Dr. Yuping Wu, Confucius Energy Storage Lab, School of Energy and Environment & Z Energy Storage Center, Southeast University, No. 2, Southeast University Road, Nanjing 211189, Jiangsu, China. E-mail: wuyp@fudan.edu.cn or wuyp@seu.edu.cn; Dr. Lili Liu, School of Energy Science and Engineering, Nanjing Tech University, Nanjing 211816, Jiangsu, China. E-mail: liulili@njtech.edu.cn; Dr. Xinhai Yuan, School of Energy Science and Engineering, Nanjing Tech University, Nanjing 211816, Jiangsu, China. E-mail: xhyuan2022@njtech.edu.cn

How to cite this article: Jia, Z.; Hou, S.; Chen, X.; Liu, L.; Yuan, X.; Fu, L.; Chen, Y.; Wu, Y. Tailoring hard carbon interfaces in carbonate-based electrolytes for sodium-ion hybrid capacitors. *Energy Mater.* **2025**, *5*, 500073. https://dx.doi.org/10.20517/energymater.2024.291

Received: 18 Dec 2024 **First Decision:** 10 Jan 2025 **Revised:** 17 Jan 2025 **Accepted:** 25 Jan 2025 **Published:** 13 Mar 2025

Academic Editor: Jiazhao Wang **Copy Editor:** Fangling Lan **Production Editor:** Fangling Lan

Abstract
The poor rate performance of hard carbon (HC) in carbonate electrolytes limits its applicability in hybrid capacitors, primarily due to the low working potential and the slow Na^+ transport kinetics within the potential plateau region. The slow desolvation of Na^+ at the electrode surface and sluggish transport of Na^+ through the solid electrolyte interface are the critical factors contributing to this issue. In this study, Co_3O_4 nanoparticles are uniformly self-grown on the HC surface to modulate the surface chemistry of HC. The introduction of Co_3O_4 not only facilitates the desolvation of Na^+ and reduces internal resistance, but also provides additional active sites for Na^+ storage as an active material. As a result of these dual effects, HC125@Co_3O_4 (a composite with an optimal Co_3O_4 loading on HC surfaces) exhibits superior rate performance and reversible capacity compared to pure HC. The sodium-ion hybrid capacitor assembled with the HC125@Co_3O_4 anode and activated carbon cathode demonstrates high energy density (129.5 Wh kg^{-1} at 583 W kg^{-1}) and high power density (26.5 Wh kg^{-1} at 11,650 W kg^{-1}), along with excellent long-time cycling stability. This study offers an effective solution to the poor rate performance and slow kinetics of HC in carbonate-based electrolytes, addressing the issue from the perspective of the electrode-electrolyte interface.

Keywords: Hard carbon, Co_3O_4, solvated structure, sodium ion, hybrid capacitors

INTRODUCTION

Nowadays, secondary batteries and supercapacitors are among the most widely used electrochemical energy storage devices[1,2]. However, batteries often suffer from relatively low power density and limited cycle life, while supercapacitors face challenges with poor energy density[3,4]. To bridge the performance gap between batteries and supercapacitors, hybrid capacitors that combine battery-type anodes with capacitor-type cathodes have emerged, leveraging the advantages of both technologies[5]. Compared to lithium-ion hybrid capacitors, sodium-ion hybrid capacitors (SICs) offer a cost advantage due to the abundant reserves of sodium[6]. Additionally, the ionic radius of the Na^+ (102 pm) is larger than that of the Li^+, which reduces the desolvation energy by 15%-20% for the same solvent molecule. The faster desolvation process, combined with the high abundance of sodium, makes it an attractive charge carrier for low-cost and high-kinetic hybrid capacitors[7-9]. Hard carbon (HC), a promising material for commercialization, has numerous active sites for Na^+ storage and a stable structure[10]. The capacity of an HC anode typically consists of a partially slope capacity above 0.1 V (*vs.* Na/Na^+) and a platform capacity below 0.1 V (*vs.* Na/Na^+)[11,12]. However, the rate performance of HC remains unsatisfactory, particularly under high currents, as the plateau capacity deteriorates rapidly. This limitation hinders the practical application of HC in hybrid capacitors.

The interaction between HC and the electrolyte is a critical factor influencing its rate performance. Electrolyte solvents for HC are primarily based on carbonate and ether solvents. Carbonate solvents are widely used in electrolyte solvents due to their excellent oxidative stability and high flash point, making them the preferred choice for high-voltage electrochemical energy storage devices. However, HC anodes for sodium-ion storage exhibit poor rate performance and low initial coulombic efficiency when matched with carbonate-based solvents. This is primarily due to the continuous growth of the solid electrolyte interphase (SEI) layer as a result of electrolyte degradation, which leads to significant kinetic challenges at the electrode/electrolyte interface, ultimately affecting the electrochemical performance[13,14]. In contrast, when ether-based electrolytes are used in HC, capacity degradation occurs more slowly as the current increases. Yi *et al.* found that the co-intercalation behavior of Na^+ and -solvent molecules in ether-based electrolytes lowers the desolvation energy, accelerating charge-transfer kinetics, particularly for Na^+ storage behavior in the platform region[15]. The SEI layer formed in ether-based electrolytes is thinner, facilitating faster Na^+ storage compared to carbonate-based electrolytes[16]. However, Yan *et al.* assessed the kinetic behavior of ether-based and carbonate-based electrolytes in the full cell composed of HC and sodium vanadium phosphate, and found that the rate performance in the carbonate-based electrolyte was superior, in contrast to conclusions drawn from conventional half-cell tests[17]. Traditional half-cell tests, with rigid cutoff criteria, overlook the overpotential and impedance of metal electrodes, leading to an underestimation of the actual capabilities of HC in carbonate-based electrolytes. Additionally, carbonate-based solvents have superior oxidative stability compared to ether-based solvents, making them better suited for the long cycle life required in hybrid capacitors[18,19]. Therefore, improving the rate performance of HC in carbonate-based solvents is crucial for meeting the practical demands of energy storage applications.

Modifying the surface chemistry of electrode materials is a widely adopted strategy to enhance the kinetics of sodium ion storage, as it directly influences the desolvation of Na^+-$(solvent)_n$ and the ability of Na^+ to migrate through the SEI layer[20-22]. For instance, increasing the surface oxygen functional groups on HC can promote electrolyte infiltration, provide more active sites for Na^+ storage, and enhance the storage kinetics of Na^+[23]. Furthermore, differences in surface conductivity between materials, such as graphite and silicon oxide, can alter the structure of the SEI layer, which in turn affects the storage performance[24]. Additionally, coating graphite with an ultrathin P layer that forms a crystalline Li_3P-based SEI during cycling has been shown to improve the desolvation of Li^+ due to its high affinity for the ion, leading to ultra-fast charging performance[25].

The introduction of nanomaterials on the surface of micrometer-sized electrode materials further optimizes surface chemistry while simultaneously increasing active sites, thereby enhancing specific capacity. Anode materials with nanostructures are particularly beneficial for hybrid capacitors, as nanosizing effectively improves kinetic performance by shortening the carrier transport path and accelerating surface charge transfer. Nanostructured materials such as TiO_2[26], Co_3O_4[27], Mo_2C[28], and CoS[29] have been successfully applied in lithium/sodium-ion hybrid capacitors. Therefore, selecting an appropriate nanostructured anode material is critical to improving the surface/interfacial chemistry of HC for hybrid capacitor applications.

Considering the findings from previous research, nanosized Co_3O_4 particles were introduced onto the HC surface as surface modification materials. The introduction of Co_3O_4 not only serves as an active material, providing more active sites, but also changes the surface chemistry of the HC anode. Through electrochemical testing and surface analysis techniques, it was found that the surface loading of Co_3O_4 increased the reversible capacity, promoted the reaction kinetics of Na^+ storage in the platform region of HC, and simultaneously reduced the desolvation energy of the HC surface. This resulted in superior overall electrochemical performance compared to pure HC. The optimal composite, HC125@Co_3O_4, exhibited a higher specific capacity of 341 m Ah g^{-1} compared to the specific capacity of 206 m Ah g^{-1} of HC. In addition, even after 500 cycles at 0.5 A g^{-1}, HC125@Co_3O_4 maintained a specific capacity of 146 mAh g^{-1}, which is higher than that of HC (104 mAh g^{-1}). In A carbonate-based electrolyte, a SIC was constructed with a HC125@Co_3O_4 anode and an activated carbon (AC) cathode, demonstrating an energy density of 54.5 Wh kg^{-1} and 76% capacity retention after 1,000 cycles at a high power density of 5,832 W kg^{-1}. Here, our work provides new insights into modulating the surface chemistry of HC anode materials in carbonate-based electrolytes to enhance its rate performance for application in hybrid capacitors.

EXPERIMENTAL

Synthesis of materials

The anode electrode materials (HC75@Co_3O_4, HC125@Co_3O_4, HC175@Co_3O_4, and Co_3O_4) were prepared using a simple one-pot solvothermal method. Except for the varying amounts of commercial HC (Fujian Yuanli Active Carbon Co., Ltd, BHC-35b) added, all other steps in the synthesis were identical. The amount of remaining H_2O in HC is about 1% by gravimetric (TG) test [Supplementary Figure 1]. The synthesis process of HC125@Co_3O_4 material is described in detail as an example. For the synthesis, 0.125 g HC powder and 0.125 g cobalt acetate powder were weighed and dissolved in 60 mL of deionized water. To this, 3 mL of ammonia solution was added, followed by stirring to ensure thorough mixing. The resulting mixed solution was then transferred to a 100 mL reaction vessel, sealed, and subjected to a 5-h reaction at 150 °C. After the reaction, the mixture was allowed to room temperature. The precipitate was washed multiple times with deionized water, and then dried in an 80 °C drying oven to obtain the final material. For the synthesis of HC75@Co_3O_4, HC175@Co_3O_4, and Co_3O_4, the masses of HC used were 0.075, 0.175, and 0 g, respectively.

Materials characterizations

X-ray diffraction (XRD, SmarLab3KW) was employed to characterize the phase and crystallinity of the synthesized powders and electrode films at different potentials. Scanning electron microscopy (SEM, Phenom proX) was used to characterize the morphology and particle size of the samples. The specific surface area (SSA), pore volume, and pore size distribution were determined by the Autosorb-IQ3 instrument, employing the Brunauer-Emmett-Teller (BET) and Barrett-Joyner-Halenda (BJH) methods. *In-situ* X-ray photoelectron spectroscopy (XPS, Thermo Scientific K-Alpha) was used to identify the surface chemical composition and electronic structure of the electrode films after two complete charge-discharge cycles. Thermal TG test (STA 449 F5) was conducted to analyze the presence and content of HC. Raman spectroscopy was performed to analyze the participation degree of the salt anion PF_6^- in the solvation structure at the electrode interface. It is worth noting that, before conducting XRD and XPS measurements, the electrodes were washed three times with dimethyl carbonate (DMC) solvent in a high-purity, argon-filled dry box to remove residual electrolyte and glass fiber membranes.

Electrochemical measurements

All anode electrode materials (HC, HC75@Co_3O_4, HC125@Co_3O_4, HC175@Co_3O_4, Co_3O_4) were prepared by mixing 70 wt% of active material, 20 wt% of conductive carbon black, and 10 wt% of polyacrylic acid (PAA) in N-methyl-2-pyrrolidone (NMP). The mixture was then coated onto copper foil and dried at 80 °C in a vacuum oven for 12 h. The mass loading of the anode electrode is approximately 1.0 mg cm^{-2}. For half-cell measurements, metallic sodium was used as the counter and reference electrode. The cathode electrode material, AC (XFNANO, XFP06), was prepared by mixing 70 wt% of active material, 20 wt% of conductive carbon black, and 10 wt% of polyvinylidene fluoride (PVDF) in NMP. The mixture was then coated onto aluminum foil and dried at 80 °C in a vacuum oven for 12 h. The mass loading of the cathode electrode is approximately 1.5 mg cm^{-2}. The HC125@Co_3O_4 anode was pre-activated by cycling at a current density of 0.05 A g^{-1} for five cycles in a Na half-cell configuration. Following pre-activation, the cell was disassembled, and the anode was used to assemble the SIC. Using the mass loading ratio (cathode:anode = 1.5:1), SIC was prepared with the HC125@Co_3O_4 anode and AC cathode. Button cells (CR2025) were assembled in an Ar-filled glovebox. Glass fiber (GF/A) was used as a separator. The electrolyte consisted of a mixture of 1.0 M $NaPF_6$ and ethylene carbonate (EC), DMC, and ethyl methyl carbonate (EMC) in a volume ratio of 1:1:1, along with 5 wt.% fluoroethylene carbonate (FEC) additive. The cycling and rate performance of the devices were tested using a battery testing system (LAND CT2001A, Wuhan, China). Cyclic voltammetry (CV, 0-3 V) and electrochemical impedance spectroscopy (EIS, 10^{-2}-10^{5} Hz) were performed using an electrochemical workstation (Chenhua, CHI760e).

Molecular dynamics simulation

Molecular dynamics (MD) simulations were performed using the COMPASS force field in Materials Studio software. To investigate the electrolyte structure in the presence of different anodes, four models were constructed. Model A consisted of 1 HC, 8 $NaPF_6$, 36 EC, 5 DMC, 30 EMC, and 5 FEC. Model B consisted of 1 Co, 8 $NaPF_6$, 36 EC, 5 DMC, 30 EMC, and 5 FEC. Model C consisted of 1 CoO, 8 $NaPF_6$, 36 EC, 5 DMC, 30 EMC, and 5 FEC. Model D consisted of 1 Co_3O_4, 8 $NaPF_6$, 36 EC, 5 DMC, 30 EMC, and 5 FEC. The charges of Na^+ and PF_6^- were scaled according to the high-frequency dielectric properties of the solvents present in the system, as proposed by researchers. For each system, initial energy minimization was performed at 0 K to obtain stable structures. Subsequently, each system underwent five cycles of annealing dynamics, with temperatures ranging between 298 and 900 K, to eliminate the presence of metastable states. Following annealing, the systems were equilibrated for 50 ps under constant temperature (298 K), constant pressure (1 bar) conditions in the NPT ensemble, termed MD equilibration. During constant-volume dynamics, coordination numbers were calculated from MD trajectories using mean square displacement analysis.

RESULTS AND DISCUSSION

The synthesis of HC125@Co_3O_4 is illustrated in Figure 1A. The defects and oxygen-containing functional groups in HC facilitate the adsorption of Co^{2+}, which act as nucleation sites for the growth of Co_3O_4[30]. Upon heating to a specific temperature, these coordinated ions decompose to form Co_3O_4 nanoparticles, which are deposited on the HC surface, resulting in the successful formation of the HC125@Co_3O_4 composite with a micro-nanostructure. HC itself exhibits an irregular block structure at the micrometer scale, while the surface of HC125@Co_3O_4 shows a more uniform distribution of Co_3O_4 particles.

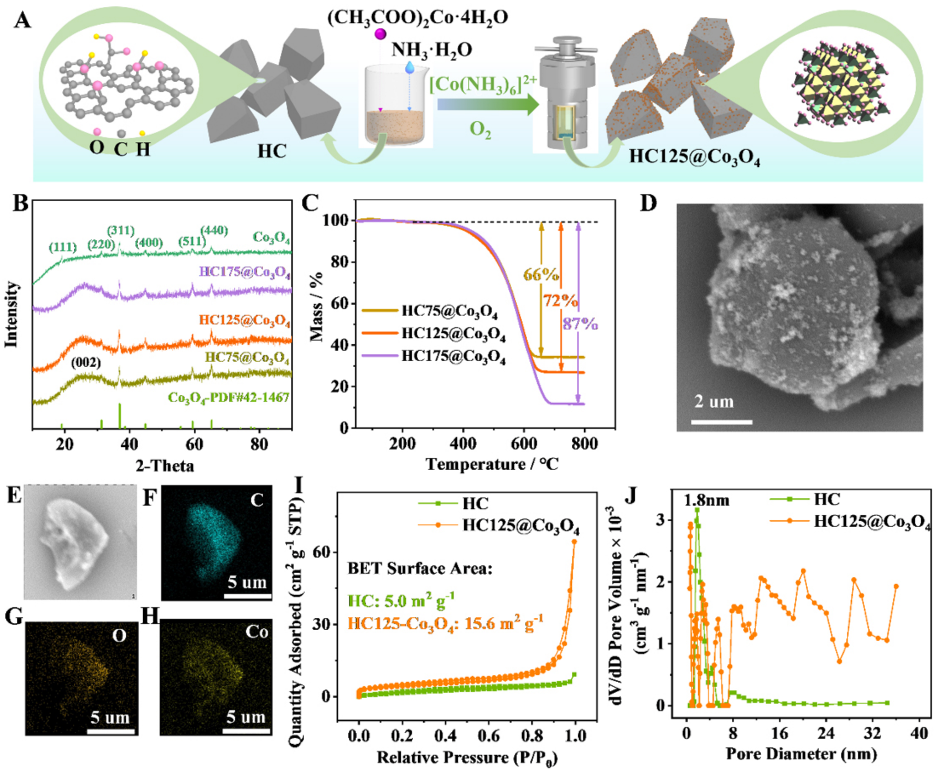

Figure 1. Schematic of the preparation process and characterization of physicochemical properties. (A) Schematic of the synthesis of HC125@Co_3O_4. (B) XRD patterns of Co_3O_4 and HC75/125/175@Co_3O_4 samples. (C) TG of HC75/125/175@Co_3O_4 samples. (D) SEM, selected area (E) and the corresponding mapping (F-H) of HC125@Co_3O_4 samples. (I) nitrogen adsorption/desorption isotherms and (J) pore size distributions of HC125@Co_3O_4 powder.

The XRD patterns clearly confirm the successful formation of HC and Co_3O_4 composite during the solvothermal process [Figure 1B]. The diffraction peaks located at 19°, 31.3°, 36.8°, 44.8°, 59.3°, and 65.2° correspond to the (110), (220), (311), (400), (511), and (440) crystal planes of Co_3O_4 (PDF#42-1467), indicating the successful synthesis of the Co_3O_4 with a face-centered cubic structure. The intensities of the (311) peaks of HC75@Co_3O_4, HC125@Co_3O_4 and HC175@Co_3O_4 are higher than that of pure Co_3O_4, indicating that the addition of HC enhances the crystallinity of Co_3O_4. The HC content in the prepared anode materials (HC75@Co_3O_4, HC125@Co_3O_4, HC175@Co_3O_4) was determined from the TG curves [Figure 1C]. The slight weight loss between 25-250 °C corresponds to the release of absorbed gases or moisture, while the decomposition of HC begins at 250 °C. The weight percentages of HC in HC75@Co_3O_4, HC125@Co_3O_4, and HC175@Co_3O_4 are 66%, 72%, and 87%, respectively, indicating the dominant presence of HC in the composite materials. Energy Dispersive X-ray Spectroscopy (EDS) elemental mapping analysis [Figure 1D-H] clearly demonstrates the uniform distribution of Co and O atoms on the surface of HC. The addition of ammonia solution does not significantly increase the N content in HC125@Co_3O_4 [Supplementary Figure 2]. From nitrogen adsorption/desorption isotherms, the N_2 isotherms for HC125@Co_3O_4 resemble type IV and H4-type hysteresis loops, indicating the presence of mesopores [Figure 1I]. Distinct peaks at 2.7, 5.4, 8.1, 12.8, 20.1, and 28.7 nm are observed in the pore size distribution for HC125@Co_3O_4 [Figure 1J]. In contrast, the N_2 isotherm of HC shows type I and H3-type hysteresis loops, indicating micropores. The pore size distribution reveals that HC125@Co_3O_4 contains a significant amount of mesoporous and microporous structures, while the SSA of HC is mainly attributed to micropores. HC125@Co_3O_4 exhibits a higher SSA compared to HC, with the increase primarily due to the successful loading of mesoporous Co_3O_4 on the surface of HC. It is important to note that micropores store

Na^+, contributing to capacity, while mesopores enhance the kinetics of Na^+ storage.

To evaluate the effect of Co_3O_4 incorporation on enhancing the electrochemical performance of the HC anode, different composite ratio materials were tested in half-cells paired with metallic sodium foils. Supplementary Figure 3 displays the CV results of HC, HC75@Co_3O_4, HC125@Co_3O_4, HC175@Co_3O_4, and Co_3O_4 at a scanning rate of 0.1 mV s^{-1} for the initial three cycles. During the first cathodic scan, two distinct irreversible peaks were observed at approximately 1.1 and 0.5 V, corresponding to the decomposition of $NaPF_6$ and solvent, respectively[31-34]. Compared to HC, the composite materials containing Co_3O_4 exhibit these two irreversible peaks at higher potentials, suggesting that solvent molecules and salt anions preferentially decompose at the Co_3O_4 layer. This early SEI formation helps prevent solvent molecules from co-intercalating with Na^+ into the HC, further indicating the successful loading of Co_3O_4 onto the HC surface. During the first anodic scan, the removal of sodium ions from the HC is observed in two steps. The first step is the disappearance of Na metal clusters in the nanopores and Na^+ de-insertion (0.22 V), while the second step involves further de-adsorption of Na^+ from the surfaces and defects (0.67 V). Multiple oxidation peaks, corresponding to the transformation of Co_3O_4 into CoO and Co_3O_4, are observed between 0.49 and 2.1 V. The CV peaks of the composite material (HC75@Co_3O_4, HC125@Co_3O_4, HC175@Co_3O_4) show a combination of the characteristic peaks from both HC and Co_3O_4. As depicted in Figure 2A, peaks A1 and A2 primarily correspond to the anodic peaks of Na^+ on HC, while peaks A3, A4, and A5 correspond to the anodic peaks of Na^+ on Co_3O_4. Furthermore, as the scanning rate increases, the CV profiles show minimal changes, indicating excellent electrochemical reversibility and robust structural stability for the composite electrode HC125@Co_3O_4. The CV profiles of the other composite electrodes also remain favorable, as shown in Supplementary Figure 4.

Galvanostatic charge/discharge (GCD) tests were performed within the potential range of 0.01-3 V (*vs.* Na/Na^+) to evaluate the electrochemical performance of the electrodes before and after composite formation, as well as for various composite ratio electrodes (HC, Co_3O_4, HC75@Co_3O_4, HC125@Co_3O_4, HC175@Co_3O_4) [Supplementary Figures 5 and 6]. Figure 2B illustrates the specific charge capacity-current density curves for these electrodes at 0.05-2 A g^{-1}. Among these, HC exhibits the lowest initial capacity, with a specific initial charge capacity of 206 mAh g^{-1} at 0.05 A g^{-1}. In contrast, Co_3O_4 demonstrates the highest initial specific charge capacity, reaching 597 mAh g^{-1}. For the composite electrodes HC75@Co_3O_4, HC125@Co_3O_4, and HC175@Co_3O_4, the initial specific charge capacity increases sequentially with the Co_3O_4 loading [Supplementary Figure 7]. After cycling at different currents, HC125@Co_3O_4 exhibits higher reversible capacity when restored to 0.05 A g^{-1}. Additionally, the reversible capacity of HC125@Co_3O_4 at 0.05-2 A g^{-1} (341-101 mAh g^{-1}) is significantly higher than that of HC (206-53 mAh g^{-1}). As observed in Figure 2C, Co_3O_4 exhibits the poorest cycling stability, with only 31 mAh g^{-1} remaining after 500 cycles at 0.5 A g^{-1}. The rapid capacity decay of Co_3O_4 is attributed to its large volume change during charge and discharge cycles. HC125@Co_3O_4 demonstrates the best cycling performance, retaining a reversible capacity of 146 mAh g^{-1} after 500 cycles, compared to 104 mAh g^{-1} for the commercial HC after the same number of cycles. Considering that Co_3O_4 comprises 28 wt% of HC125@Co_3O_4, the capacity contribution ratios of Co_3O_4 in HC125@Co_3O_4 are 60%, 26%, 14%, and 5%, respectively, at the 1st, 100th, 200th, and 500th cycles. These results indicate that HC125@Co_3O_4 is the best anode among all materials, with the capacity advantage of Co_3O_4 in HC125@Co_3O_4 being most pronounced during the first 200 charge-discharge cycles.

As shown in Figure 2D, the pseudocapacitive contribution of HC125@Co_3O_4 at scan rates of 0.1-1.0 mV s^{-1} is calculated to range from 38% to 66%, indicating its pseudocapacitive-dominant kinetic behavior in sodium-based energy storage devices. Although the introduction of the battery-type material Co_3O_4 reduces the pseudocapacitance contribution ratio of the HC (55%-79%) electrode material, pseudocapacitive-

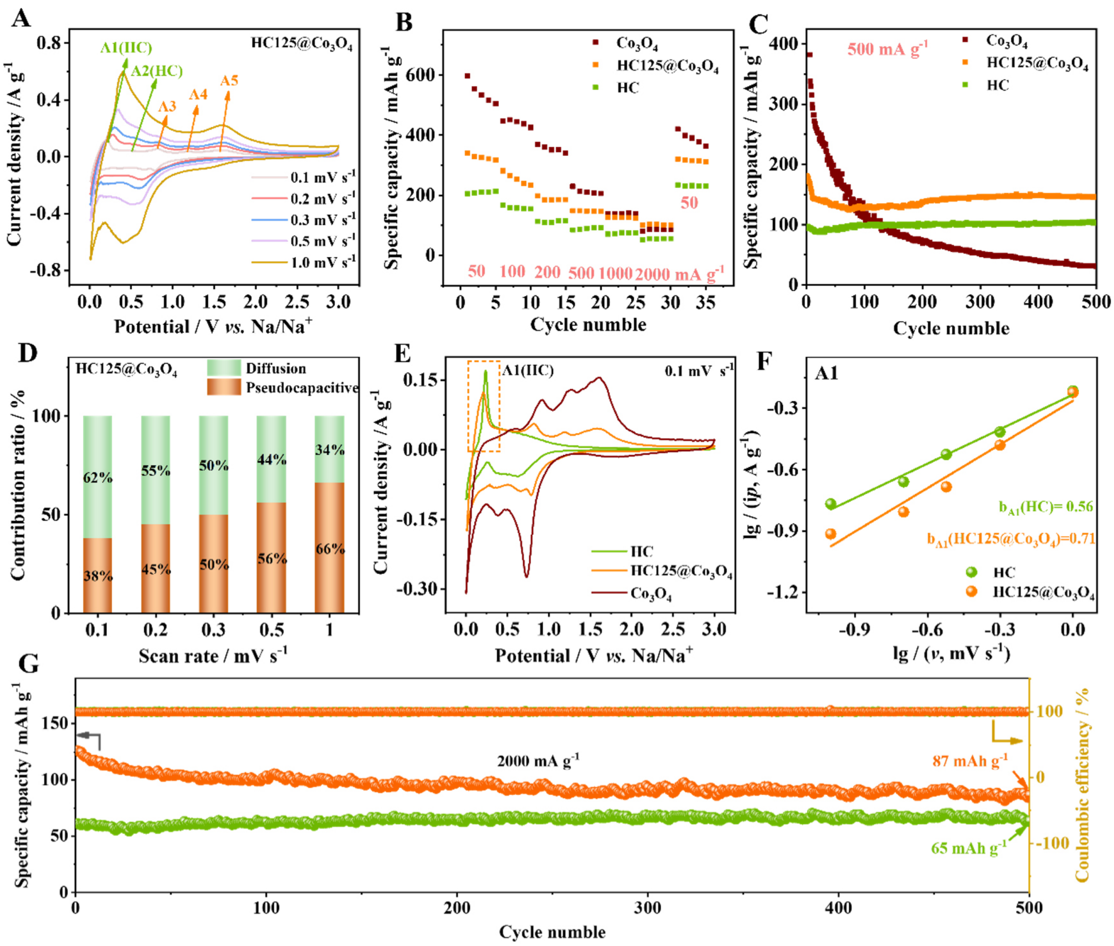

Figure 2. Electrochemical performance tests. (A) CV plots of HC125@Co_3O_4, (B) rate capability, and (C) cycling performance of HC, HC125@Co_3O_4 and Co_3O_4 samples. (D) pseudocapacitive contribution. (E) CV plots for the first cycle, (F) the relationship of lg*i vs.* lg*v* (A1), and (G) cycling stability at 2 A g^{-1} of HC and HC125@Co_3O_4 electrode.

dominant kinetic behavior still prevails overall [Supplementary Figure 8]. Furthermore, the kinetic *b*-values of A3, A4 and A5 oxidation peaks associated with Co_3O_4 are 0.62, 0.66 and 0.70, respectively, confirming that the nanosized Co_3O_4 contributes to both pseudocapacitive and diffusive behaviors, enhancing the overall performance of the electrodes [Supplementary Figure 9].

Additionally, for HC electrode materials, the disappearance of quasi-metallic Na^+ clusters in nanopores and their de-insertion from the interlayers, corresponding to the plateau capacity (A1), are the rate-limiting steps that influence the kinetic dynamics of Na^+ storage [Figure 2E]. Based on the relationship between the measured peak current (i) and scan rate (v): $i = av^b$, where a and b are constants. The *b*-value of peak A1 for HC125@Co_3O_4 is 0.71, while the *b*-value of HC (A1) is 0.56 [Figure 2F]. This suggests that the introduction of Co_3O_4 promotes the kinetics of Na^+ in the platform region, thereby enhancing the reversible capacity of HC. As shown in Figure 2C and G, HC125@Co_3O_4 maintains a higher reversible capacity than HC even after 500 cycles.

The shift of the two irreversible peaks to higher potentials indicates that the loading of Co_3O_4 onto HC promotes the early formation of the SEI film. The alteration may influence the ability of Na^+ to de-solvate and pass through the SEI. To further investigate this, the impedance curves of HC//Na and

HC125@Co_3O_4//Na batteries after five cycles were fitted using the Arrhenius equation at different temperatures, and the energy barriers for overcoming the SEI film and the desolvation process were analyzed[35-37]:

$$k = \frac{1}{R_{\mathrm{SEI/ct}}} = A \exp\left(-\frac{E_a}{RT}\right) \tag{1}$$

Which can also be transformed into:

$$\ln\left(\frac{1}{R_{\mathrm{SEI}/ct}}\right) = \ln(A) - \frac{E_a}{RT} \tag{2}$$

where k is the rate constant, $R_{SEI/ct}$ represents the SEI film resistance (R_{SEI}) or charge transfer resistance (R_{ct}), A is the frequency coefficient, R is the ideal gas constant, T is the absolute temperature, and E_a is the reaction activation energy. In the Nyquist plots of Figure 3A and B, the R_{SEI} values of HC at temperatures 263, 273, 283, 293, and 303 K are 288.5, 151.6, 90.3, 61.1, and 38.9 Ω, respectively, while for HC125@Co_3O_4, the R_{SEI} values are 103.5, 54.8, 37.1, 29.8, and 18.7 Ω. The equivalent circuit diagram used for fitting is shown in Figure 3C. Based on the calculation of Eq. (2), the activation energy for Na^+ passing through SEI in HC125@Co_3O_4 is 27(2) kJ mol^{-1}, which is lower than that of the HC (32.7(1.2) kJ mol^{-1}) [Figure 3D]. This indicates that the SEI film formed at the interface of Co_3O_4-loaded HC can effectively enhance the diffusion rate of Na^+.

Furthermore, the R_{ct} values of HC and HC125@Co_3O_4 at different temperatures are shown in Figure 3A and B. For HC, the R_{ct} values are 5,048.2, 1,575.1, 558.4, 301.9, and 106.3 Ω, respectively; for the HC125@Co_3O_4, the values are 3011.0, 842.5, 386.5, 227.1, and 85.8 Ω, respectively. The activation energy, derived from the fitting R_{ct}, represents the desolvation energy of sodium ions. As shown in Figure 3E, the surface loading of Co_3O_4 reduces the desolvation energy of HC from 62(3) to 55(3) kJ mol^{-1}. At various temperatures, both the R_{SEI} and R_{ct} of HC125@Co_3O_4 are lower than those of commercial HC. Compared with HC, the surface loading of Co_3O_4 reduces the energy required for Na^+ to pass through the SEI film by 17%(10%) and the energy of the Na^+ desolvation by 11%(10%), which significantly contributes to the enhanced electrochemical performance of HC.

The change in desolvation energy is linked to the solvation structure of Na^+ on the electrode surface, and Raman spectroscopy is a common method for studying the solvation structure. To simulate the state of the electrode sheets in the battery, the HC and HC125@Co_3O_4 sheets were soaked in the electrolyte overnight before performing Raman testing. Figure 3F illustrates the changes in the participation of anionic PF_6^- in the solvation structure at the interface of HC and HC125@Co_3O_4.

The peak of Na^+-PF_6^- in pure $NaPF_6$ is present at 761 cm^{-1}. The peak located at 717 cm^{-1} represents the presence of EC molecules ($O_{o\text{-}c\text{-}o}$) with ring respiration[38]. The peak around 739 cm^{-1} represents the stretching vibration of PF_6^- ($V_{P\text{-}F}$). PF_6^- at the interface can generally be categorized into three types: free ions (SSIP), contact ion pairs (CIP, where one PF_6^- coordinated with one Na^+), and aggregated clusters (AGG, where one PF_6^- coordinated with two or more Na^+)[39]. The $V_{P\text{-}F}$ of PF_6^- at 739.1 cm^{-1} in the electrolyte at the HC125@Co_3O_4 interface exhibits the smallest redshift, which is higher than those observed at the HC (737.7 cm^{-1}) and Co_3O_4 (738.4 cm^{-1}) interfaces. This suggests a higher content of CIP and AGG in HC125@Co_3O_4. Compared to HC, the introduction of Co_3O_4 alters the solvent structure of the HC interface, with more PF_6^- participating in the interfacial solvent structure. As a result, during the desolvation process

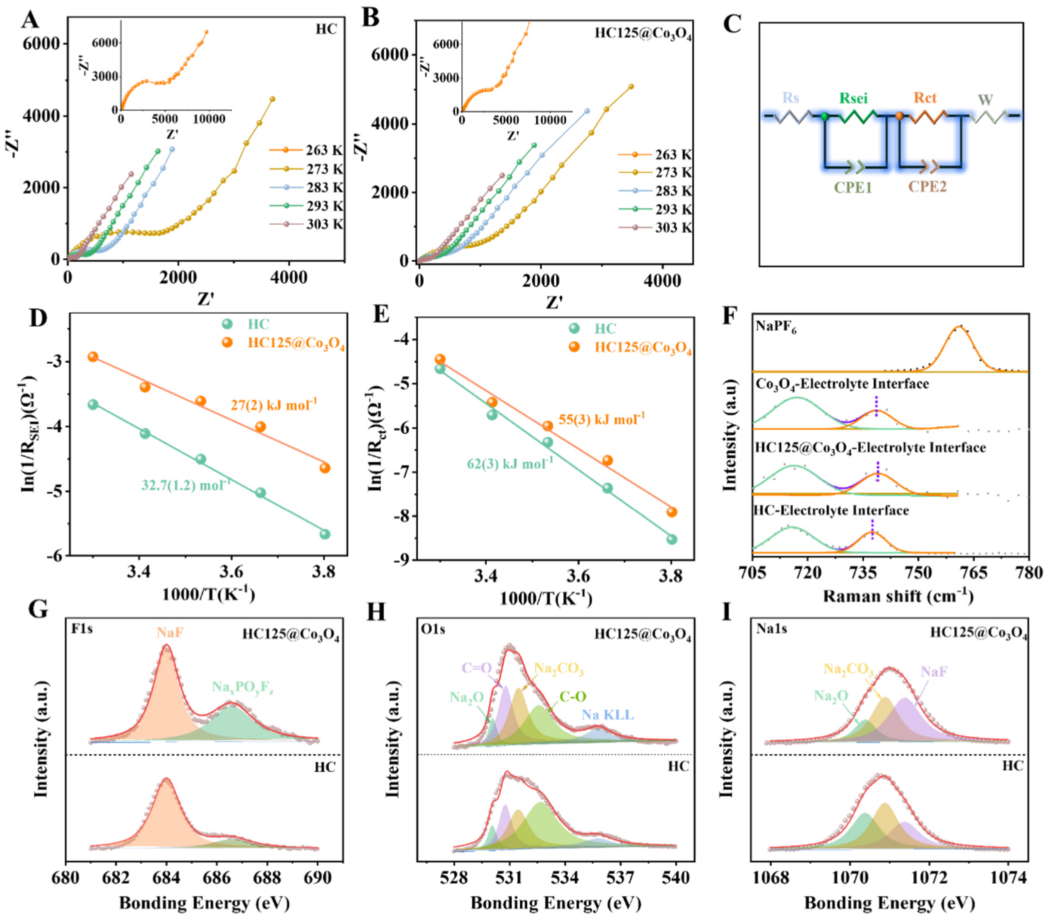

Figure 3. Electrochemical impedance and surface characterization of HC and HC125@ Co_3O_4. EIS plots at different temperatures of (A) HC and (B) HC125@Co_3O_4, and (C) the corresponding equivalent circuits. Arrhenius fitted lines for (D) R_{SEI} and (E) R_{ct} of HC and HC125@Co_3O_4. (F) Raman fitted plots of $NaPF_6$, HC, Co_3O_4, HC125@Co_3O_4. XPS spectra of (G) F1s, (H) O1s and (I) Na1s for HC and HC125@Co_3O_4 in sodium intercalated state after five cycles.

at the HC125@Co_3O_4 interface, more salt anions decompose to form an SEI film enriched with NaF[40-42]. The NaF-rich SEI film enhances the desolvation ability of Na^+, mainly by weakening the interaction between Na^+ and solvents[43]. Furthermore, the high content of NaF reduces the activation energy of the SEI formation and interfacial charge transfer resistance, thereby improving the reversible capacity of HC at high currents.

To confirm that the introduction of Co_3O_4 nanocrystals alters the composition of the SEI, XPS analysis was conducted on the electrodes of HC and HC125@Co_3O_4 after five cycles, respectively. As shown in Figure 3G, the peaks in the F1s spectrum primarily correspond to the decomposition products of the anions in $NaPF_6$. Compared to HC, the SEI film on the surface of HC125@Co_3O_4 contains higher amounts of $Na_xPO_yF_z$ (686.6 eV) and NaF (684 eV), indicating that the introduction of Co_3O_4 promotes the decomposition of the PF_6^- anion. The products of the reaction between $NaPF_6$ and Na_2CO_3 are $Na_xPO_yF_z$ and NaF[44]. The organic polymer $Na_xPO_yF_z$ can effectively inhibit electrolyte decomposition, while NaF is recognized for its ability to enhance the rapid transport of sodium ions. The combination of these two components improves both the sodium ion conductivity of the SEI and the cycling stability of the electrode material.

The fitting of O1s shown in Figure 3H reveals peaks located at 530.1, 530.8, 531.5, and 532.7 eV, corresponding to Na_2O, C=O, Na_2CO_3, and C-O, respectively[45]. The C-O peak is generally associated with organic components in the SEI. The lower C-O content in HC125@Co_3O_4 compared to HC indicates that the presence of Co_3O_4 reduces the generation of soluble organic components, such as $NaCO_2R$, within the SEI. From the Na1s [Figure 3I], the NaF content in HC125@Co_3O_4 is higher than that in HC, consistent with the conclusions obtained from Figure 3G.

Considering the charge storage mechanism of the Co_3O_4 conversion reaction, it is essential to discuss the components formed after the conversion reaction and how each component influences the Na^+ solvation structure. To explore this, a series of *ex-situ* XRD and XPS analyses were conducted to investigate the mechanism of HC125@Co_3O_4 as the anode and the composition of the electrode surface. Figure 4A shows the changes in the pristine electrode and the electrode at different potentials during the second GCD cycle [Figure 4B]. In the XRD spectrum of the pristine HC125@Co_3O_4, strong diffraction peaks corresponding to the spinel structure of Co_3O_4, such as (111), (220), and (311), are clearly visible. Since the XRD test was performed on HC125@Co_3O_4 coated on copper foil, the diffraction peaks from Co_3O_4 are relatively weak due to the strong diffraction signal from the collector (Cu foil). However, the peaks from crystal surfaces with high intensity are still distinguishable. In the magnified region between 35°-40°, it is evident that the (311) crystal plane disappears during the second charging/discharging process, indicating that Co_3O_4 has transformed into Co-based species with an amorphous state after sodiation. Additionally, NaF peaks are clearly observed, suggesting the presence of an SEI layer rich in NaF on the surface of HC125@Co_3O_4. This NaF-rich SEI layer provides excellent electronic isolation capability and reduces sodium diffusion resistance, thereby accelerating the kinetics of sodium ion transfer[46]. Regarding the Co-based species formed after the transformation of Co_3O_4, *ex-situ* XPS analysis was performed [Figure 4C]. It can be seen that the main peak of $Co2p_{3/2}$ shifts at different stages of the second GCD cycle: at the onset of discharge (3V-D), fully-discharged (0.01V-C), and fully-charged (3V-C). During discharging, the binding energy of the $Co2p_{3/2}$ peak decreased (from 780.4 to 780.1 eV), and increased again during recharge (from 780.1 to 780.3 eV), indicating a change in the relative proportion of Co-based species on the electrode surface. The $Co2p_{3/2}$ spectrum can be convoluted into multiple distinguishable peaks: the peak at 779.3 eV corresponds to metallic Co, while peaks at 780.5 and 782.1 eV correspond to Co_3O_4 and CoO, respectively. During discharge, the content of Co species increases, while the content of CoO species remains nearly unchanged. This suggests that CoO transforms into Co, and part of Co_3O_4 also converts into CoO and Co species during discharge. Conversely, during charging, the content of Co decreases while the content of CoO increases, indicating the transformation from Co to CoO. These results demonstrate that three cobalt-based species (Co, CoO and Co_3O_4) are present during the charge/discharge process, and their relative proportions change accordingly.

The storage characteristics of Na^+ in HC and the dynamic changes at the SEI interface were further explored through C1s XPS analysis, as shown in Figure 4D. The peak at 283.2 eV, corresponding to an extremely low binding energy, is attributed to Na_x-HC[47]. The peak at 287.5 eV corresponds to the C=O bond. The intensity of this C=O peak decreases as Na^+ is absorbed by the HC (during discharge) and increases again during Na^+ extraction (during charge), indicating the reversible reaction between C=O and Na^+[48]. The peak at 288.7 eV corresponds to $-CO_3^-$, representing SEI film components such as Na_2CO_3 and $NaOCO_2R$. The intensity of this peak increases during discharge and decreases during charge, suggesting dynamic changes in the SEI film during the early cycles and indicating potential for SEI regulation.

To confirm the influence of three species formed after Co_3O_4 conversion on the Na^+ solvation sheath, classic MD simulations were performed. The Raman tests show different Na^+ solvation structures on the overall

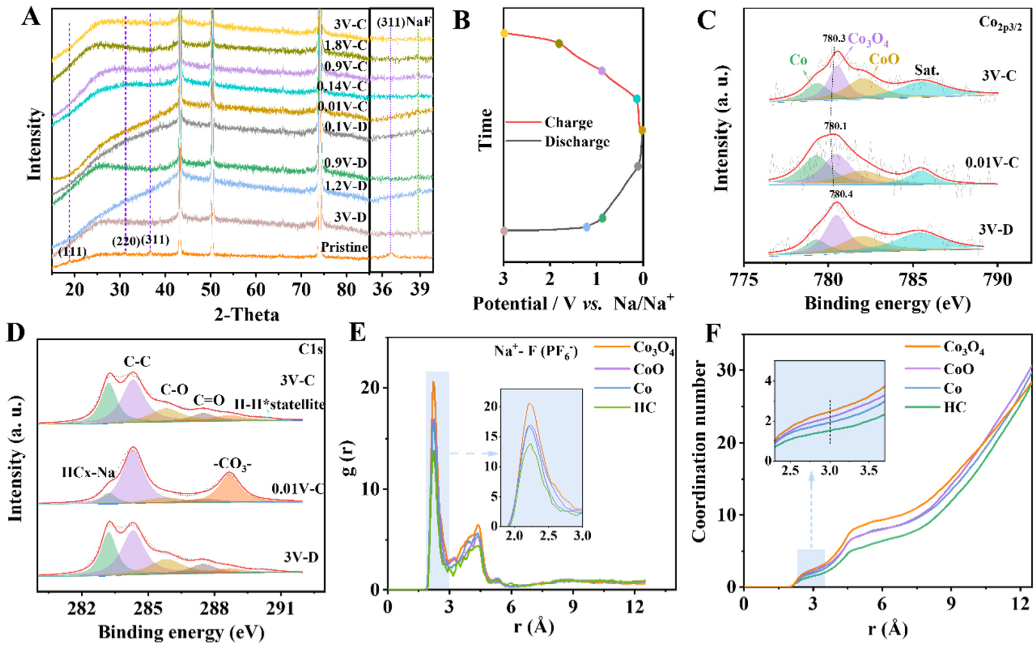

Figure 4. Structural and surface evolution of HC125@ Co_3O_4 during cycling. (A) *Ex situ* XRD of the pristine electrode and HC125@Co_3O_4 electrode at different potentials during the second cycle at 0.05 A g^{-1} (C/D mean charge/discharge), and (B) the corresponding potential and GCD curves. *Ex situ* XPS spectra of (C) $Co_{2p3/2}$ and (D) C1s for HC125@Co_3O_4 electrode in pristine, fully discharged-0.01 V and charged-3 V states during the second discharging/charging cycles at 0.05 A g^{-1}.(E) RDF and coordination number of Na^+-PF_6^- in the presence of HC, Co, CoO and Co_3O_4.

electrode surface, while MD calculations further present the effects of various species in the electrode material on the Na^+ solvation, complementing the Raman results. In the initial stages of sodium ion storage, Co_3O_4 mainly exists as three species: Co_3O_4, CoO, and Co. To better understand the influence of Co-based species on the coordination between Na^+ and PF_6^-, four models were constructed [Supplementary Figure 10]. Figure 4E shows the radial distribution function (RDF) of Na^+-PF_6^- in the electrolyte in the presence of four materials (Co_3O_4, CoO, Co, HC). The peak at 2.23 Å represents the first solvation sheath of Na^+, corresponding to the Na^+-PF_6^- coordination structure. In the presence of Co-based species, this peak value is higher compared to HC, with Co_3O_4 showing the highest peak value. The intensity of this peak in the presence of Co-based species is greater than that of HC in all cases, with Co_3O_4 exhibiting the largest peak. This change in peak intensity indicates that the presence of Co-based species enhances the coordination ability of Na^+-PF_6^-, which is consistent with the findings from Raman spectroscopy. Figure 4F shows the coordination numbers derived from RDF. In the primary solvation shell of Na^+, the coordination number of PF_6^- in the presence of HC is 1.53. In contrast, in the presence of Co-based species, the average coordination numbers of PF_6^- are all greater than 1.53, with values of 1.94 (Co), 2.19 (CoO), and 2.49 (Co_3O_4), respectively. The increase in coordination numbers further supports the idea that the surface loading of Co_3O_4 regulates the solvation structure of Na^+, promoting more PF_6^- to participate in coordination and thereby contributing to the formation of an SEI film enriched with NaF.

To assess the practicality of HC125@Co_3O_4 in SICs, the SIC comprising HC125@Co_3O_4 anode and AC cathode (HC125@Co_3O_4//AC) was assembled, based on the operating principle shown in Figure 5A. During charge and discharge processes, the HC125@Co_3O_4 anode undergoes the sodiation/desodiation, while the AC cathode facilitates the adsorption/desorption of PF_6^- on its surface. The operating voltage window was optimized to be 0.01-3.8 V to avoid side reactions [Figure 5B]. The CV curves of SIC devices, tested at scan rates of 2 to 50 mV s^{-1}, show minimal deviation from ideal rectangle shapes, reflecting the combined energy

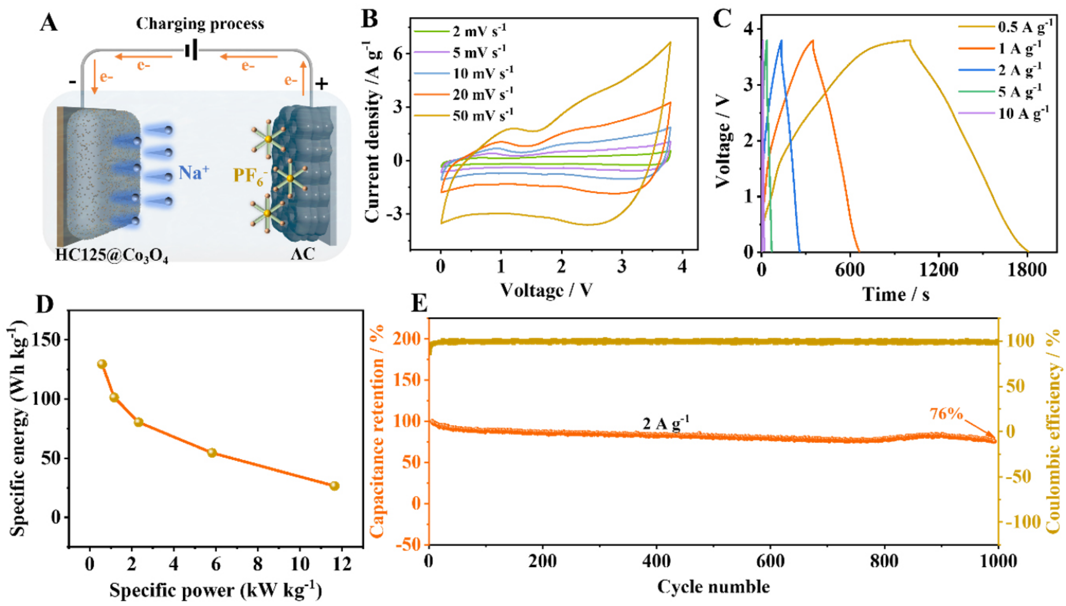

Figure 5. Electrochemical performance of HC125@Co_3O_4//AC sodium-ion hybrid capacitor (SIC) (A) The schematics of work principles during the charging process, (B) CV plots, (C) GCD curves, (D) Ragone plots and (E) cycling performance of HC125@Co_3O_4//AC SIC.

storage mechanism of the anode and cathode. Figure 5C displays the GCD curves, which exhibit quasi-triangular shapes, further indicating multiple energy storage mechanisms in the device. The Ragone plot of the HC125@Co_3O_4//AC SIC [Figure 5D] was calculated based on the total mass of the cathode and anode, achieving an energy density of 129.5 Wh kg^{-1} at a power density of 583 W kg^{-1}. Notably, even at an ultra-high power density of 11,650 W kg^{-1}, the SIC device maintains an energy density of 26.5 Wh kg^{-1}, which offers a higher power density compared to the latest literature, as shown in Supplementary Table 1. The HC125@Co_3O_4//AC also demonstrates excellent cycling stability [Figure 5E], with a capacity retention rate of 76% after 1,000 cycles at 2.0 A g^{-1}. The above SIC highlights the promising potential of HC125@Co_3O_4 as an anode material for advanced sodium-based energy storage devices and also underscores the application prospects of commercial HC in hybrid capacitors.

CONCLUSIONS

To enhance the rate performance and Na^+ reaction kinetics of HC in carbonate-based electrolytes, Co_3O_4 nanoparticles were uniformly loaded onto the surface of HC via a simple one-step solvothermal method. As an active material, Co_3O_4 not only contributes to an increase in reversible specific capacity but also regulates the Na^+ solvation structure on the electrode surface. After 200 cycles, the NaF-rich SEI plays a dominant role in improving the capacity of HC. The presence of Co-based species facilitates greater participation of PF_6^- in Na^+ coordination, promotes Na^+ desolvation, and optimizes the composition of the SEI film. In the SEI of HC125@Co_3O_4, the NaF content is higher than in HC, leading to faster charge transfer kinetics. As a result, HC125@Co_3O_4 exhibits an excellent reversible capacity of 341 mAh g^{-1} at 0.05 A g^{-1}, and retains a high capacity of 87 mAh g^{-1} after 500 cycles at 2 A g^{-1}. The assembled SIC achieves a maximum energy density of 129.5 Wh kg^{-1} and a maximum power density of 11,650 W kg^{-1}, with a capacity retention rate of 76% after 1,000 cycles at 2 A g^{-1}. This work provides a novel strategy for regulating the solvation environment of sodium ions and promotes the practical application progress of battery-type HC materials in hybrid capacitors.

DECLARATIONS

Acknowledgments

The authors gratefully acknowledge Project on Carbon Emission Peak and Neutrality of Jiangsu Province, the financial support from the National Key R & D Program of China, NSFC Key Project, and Cultivation Program for The Excellent Doctoral Dissertation of Nanjing Tech University.

Authors' contributions

Investigation, writing-original draft: Jia, Z.
Formal analysis: Hou, S.; Chen, X.
Data visualization: Fu, L.; Chen, Y.
Review, supervision, funding acquisition: Liu, L.; Yuan, X.; Wu, Y.

Availability of data and materials

Supplementary Material is available from the authors.

Financial support and sponsorship

This work was supported by from the Project on Carbon Emission Peak and Neutrality of Jiangsu Province (BE2022031-4), the National Key R & D Program of China (2021YFB2400400), NSFC Key Project (52073143, 52131306, and 52122209), and Cultivation Program for The Excellent Doctoral Dissertation of Nanjing Tech University.

Conflicts of interest

Wu, Y., the Editor-in-Chief of *Energy Materials*, and Chen, Y., an Associate Editor of the journal, were not involved in any stage of the editorial process, including reviewer selection, manuscript handling, or decision-making, while the other authors have declared that they have no conflicts of interest.

Ethical approval and consent to participate

Not applicable.

Consent for publication

Not applicable.

REFERENCES

1. Simon, P.; Gogotsi, Y.; Dunn, B. Where do batteries end and supercapacitors begin? *Science* **2014**, *343*, 1210-1. DOI PubMed
2. Dong, S.; Lv, N.; Wu, Y.; Zhu, G.; Dong, X. Lithium-ion and sodium-ion hybrid capacitors: from insertion-type materials design to devices construction. *Adv. Funct. Mater.* **2021**, *31*, 2100455. DOI
3. Raza, W.; Ali, F.; Raza, N.; et al. Recent advancements in supercapacitor technology. *Nano. Energy.* **2018**, *52*, 441-73. DOI
4. Yuan, X.; Yuan, X.; Zhang, S.; et al. An aqueous rechargeable Al-ion battery based on cobalt hexacyanoferrate and Al metal. *Adv. Energy. Mater.* **2024**, *14*, 2302712. DOI
5. Wang, H.; Zhu, C.; Chao, D.; Yan, Q.; Fan, H. J. Nonaqueous hybrid lithium-ion and sodium-ion capacitors. *Adv. Mater.* **2017**, *29*, 1702093. DOI
6. Eshetu, G. G.; Elia, G. A.; Armand, M.; et al. Electrolytes and interphases in sodium-based rechargeable batteries: recent advances and perspectives. *Adv. Energy. Mater.* **2020**, *10*, 2000093. DOI
7. Ponrouch, A.; Monti, D.; Boschin, A.; Steen, B.; Johansson, P.; Palacín, M. R. Non-aqueous electrolytes for sodium-ion batteries. *J. Mater. Chem. A.* **2015**, *3*, 22-42. DOI
8. Jónsson, E.; Johansson, P. Modern battery electrolytes: ion-ion interactions in Li^+/Na^+ conductors from DFT calculations. *Phys. Chem. Chem. Phys.* **2012**, *14*, 10774-9. DOI
9. Okoshi, M.; Yamada, Y.; Yamada, A.; Nakai, H. Theoretical analysis on de-solvation of lithium, sodium, and magnesium cations to

organic electrolyte solvents. *J. Electrochem. Soc.* **2013**, *160*, A2160-5. DOI

10. Lu, Z.; Yin, X.; Ji, Y.; et al. Modulating the graphitic domains of hard carbons via tuning resin crosslinking degree to achieve high rate and stable sodium storage. *Energy. Mater.* **2024**, *4*, 400038. DOI
11. Wang, Z.; Feng, X.; Bai, Y.; et al. Probing the energy storage mechanism of quasi-metallic na in hard carbon for sodium-ion batteries. *Adv. Energy. Mater.* **2021**, *11*, 2003854. DOI
12. Sun, N.; Qiu, J.; Xu, B. Understanding of sodium storage mechanism in hard carbons: ongoing development under debate. *Adv. Energy. Mater.* **2022**, *12*, 2200715. DOI
13. Bouibes, A.; Takenaka, N.; Fujie, T.; Kubota, K.; Komaba, S.; Nagaoka, M. Concentration effect of fluoroethylene carbonate on the formation of solid electrolyte interphase layer in sodium-ion batteries. *ACS. Appl. Mater. Interfaces.* **2018**, *10*, 28525-32. DOI PubMed
14. Xia, H.; Zan, L.; Qu, G.; et al. Evolution of a solid electrolyte interphase enabled by FeN_X/C catalysts for sodium-ion storage. *Energy. Environ. Sci.* **2022**, *15*, 771-9. DOI
15. Yi, X.; Li, X.; Zhong, J.; et al. Unraveling the mechanism of different kinetics performance between ether and carbonate ester electrolytes in hard carbon electrode. *Adv. Funct. Mater.* **2022**, *32*, 2209523. DOI
16. Yang, J.; Ruan, J.; Li, Q.; et al. Improved low-temperature performance of rocking-chair sodium-ion hybrid capacitor by mitigating the de-solvation energy and interphase resistance. *Adv. Funct. Mater.* **2022**, *32*, 2200566. DOI
17. Yan, L.; Zhang, G.; Wang, J.; et al. Revisiting electrolyte kinetics differences in sodium ion battery: are esters really inferior to ethers? *Energy. Environ. Mater.* **2023**, *6*, e12523. DOI
18. Kang, H. J.; Huh, Y. S.; Im, W. B.; Jun, Y. S. Molecular cooperative assembly-mediated synthesis of ultra-high-performance hard carbon anodes for dual-carbon sodium hybrid capacitors. *ACS. Nano.* **2019**, *13*, 11935-46. DOI PubMed
19. Wang, C.; Zhao, N.; Li, B.; et al. Pseudocapacitive porous hard carbon anode with controllable pyridinic nitrogen and thiophene sulfur co-doping for high-power dual-carbon sodium ion hybrid capacitors. *J. Mater. Chem. A.* **2021**, *9*, 20483-92. DOI
20. Wang, E.; Wan, J.; Guo, Y. J.; et al. Mitigating electron leakage of solid electrolyte interface for stable sodium-ion batteries. *Angew. Chem. Int. Ed.* **2023**, *62*, e202216354. DOI
21. Lv, Z.; Li, T.; Hou, X.; et al. Solvation structure and solid electrolyte interface engineering for excellent Na^+ storage performances of hard carbon with the ether-based electrolytes. *Chem. Eng. J.* **2022**, *430*, 133143. DOI
22. Yang, J.; Long, K.; Guo, Z.; et al. Synergetic modulation on solvation structure and electrode interface to achieve lithium-ion batteries cycled at ultra-low temperature. *Chem. Eng. J.* **2023**, *473*, 145455. DOI
23. Shen, C.; Wang, C.; Jin, T.; Zhang, X.; Jiao, L.; Xie, K. Tailoring the surface chemistry of hard carbon towards high-efficiency sodium ion storage. *Nanoscale* **2022**, *14*, 8959-66. DOI
24. Lee, C. R.; Jang, H. Y.; Leem, H. J.; et al. Surface work function-induced thermally vulnerable solid electrolyte interphase formation on the negative electrode for lithium-ion batteries. *Adv. Energy. Mater.* **2024**, *14*, 2302906. DOI
25. Tu, S.; Zhang, B.; Zhang, Y.; et al. Fast-charging capability of graphite-based lithium-ion batteries enabled by Li_3P-based crystalline solid-electrolyte interphase. *Nat. Energy.* **2023**, *8*, 1365-74. DOI
26. Huo, J.; Xiao, Y.; Yang, H.; Yue, G.; Fang, Y.; Guo, S. Ultrasmall TiO_2/C nanoparticles with oxygen vacancy-enriched as an anode material for advanced Li-ion hybrid capacitors. *J. Energy. Storage.* **2024**, *89*, 111586. DOI
27. Peng, Y.; Liu, H.; Li, Y.; Song, Y.; Zhang, C.; Wang, G. Embedding Co_3O_4 nanoparticles in three-dimensionally ordered macro-/mesoporous TiO_2 for Li-ion hybrid capacitor. *J. Colloid. Interface. Sci.* **2021**, *596*, 130-8. DOI
28. Jiang, Y.; Wang, H.; Dong, J.; et al. Mo_2C nanoparticles embedded in carbon nanowires with surface pseudocapacitance enables high-energy and high-power sodium ion capacitors. *Small* **2022**, *18*, e2200805. DOI
29. Yang, Y.; Ma, Y.; Wang, X.; Gao, Z.; Yu, J.; Liu, T. In-situ evolution of CoS/C hollow nanocubes from metal-organic frameworks for sodium-ion hybrid capacitors. *Chem. Eng. J.* **2023**, *455*, 140610. DOI
30. Dong, Y.; He, K.; Yin, L.; Zhang, A. A facile route to controlled synthesis of Co_3O_4 nanoparticles and their environmental catalytic properties. *Nanotechnology* **2007**, *18*, 435602. DOI
31. Huang, S.; Yang, L.; Xu, G.; et al. Hollow Co_3O_4@N-doped carbon nanocrystals anchored on carbon nanotubes for freestanding anode with superior Li/Na storage performance. *Chem. Eng. J.* **2021**, *415*, 128861. DOI
32. Yin, X.; Yin, Y.; Wang, N.; et al. Facile fabrication of a series of Cu-doped Co_3O_4 with controlled morphology for alkali metal-ion batteries. *Colloids. Surf. A.* **2023**, *656*, 130459. DOI
33. Ma, M.; Cai, H.; Xu, C.; et al. Engineering solid electrolyte interface at nano-scale for high-performance hard carbon in sodium-ion batteries. *Adv. Funct. Mater.* **2021**, *31*, 2100278. DOI
34. Liu, M.; Wu, F.; Gong, Y.; et al. Interfacial-catalysis-enabled layered and inorganic-rich SEI on hard carbon anodes in ester electrolytes for sodium-ion batteries. *Adv. Mater.* **2023**, *35*, e2300002. DOI
35. Song, G.; Yi, Z.; Su, F.; et al. Boosting the low-temperature performance for Li-ion batteries in $LiPF_6$-based local high-concentration electrolyte. *ACS. Energy. Lett.* **2023**, *8*, 1336-43. DOI
36. Lu, Z.; Geng, C.; Yang, H.; et al. Step-by-step desolvation enables high-rate and ultra-stable sodium storage in hard carbon anodes. *Proc. Natl. Acad. Sci. USA.* **2022**, *119*, e2210203119. DOI PubMed PMC
37. Huang, X.; Wang, M.; Wang, Q.; et al. Acceleration of interfacial kinetics induced by regulation of Li^+ desolvation process in lithium metal-based batteries. *J. Power. Sources.* **2024**, *592*, 233884. DOI
38. Yang, G.; Ivanov, I. N.; Ruther, R. E.; et al. Electrolyte solvation structure at solid-liquid interface probed by nanogap surface-

enhanced raman spectroscopy. *ACS. Nano.* **2018**, *12*, 10159-70. DOI

39. Cai, T.; Sun, Q.; Cao, Z.; et al. Electrolyte additive-controlled interfacial models enabling stable antimony anodes for lithium-ion batteries. *J. Phys. Chem. C.* **2022**, *126*, 20302-13. DOI
40. Umesh, B.; Chandra, R. P.; Hernandha, R. F. H.; et al. Moderate-concentration fluorinated electrolyte for high-energy-density Si//$LiNi_{0.8}Co_{0.1}Mn_{0.1}O_2$ batteries. *ACS. Sustain. Chem. Eng.* **2020**, *8*, 16252-61. DOI
41. Hai, F.; Yi, Y.; Guo, J.; et al. Indirect regulation of solvation structure in all-fluorinated electrolyte by introducing carboxylate for stable 5 V battery. *Chem. Eng. J.* **2023**, *472*, 144993. DOI
42. Pham, T. D.; Bin, F. A.; Nguyen, H. D.; Oh, H. M.; Lee, K. Enhanced performances of lithium metal batteries by synergistic effect of low concentration bisalt electrolyte. *J. Mater. Chem. A.* **2022**, *10*, 12035-46. DOI
43. Li, W.; Guo, X.; Song, K.; et al. Binder-induced ultrathin SEI for defect-passivated hard carbon enables highly reversible sodium-ion storage. *Adv. Energy. Mater.* **2023**, *13*, 2300648. DOI
44. Spotte-smith, E. W. C.; Petrocelli, T. B.; Patel, H. D.; Blau, S. M.; Persson, K. A. Elementary decomposition mechanisms of lithium hexafluorophosphate in battery electrolytes and interphases. *ACS. Energy. Lett.* **2023**, *8*, 347-55. DOI
45. Li, Z.; Li, Y.; Bi, C.; et al. Construction of organic-rich solid electrolyte interphase for long-cycling lithium-sulfur batteries. *Adv. Funct. Mater.* **2024**, *34*, 2304541. DOI
46. Lu, Y.; Zhang, W.; Liu, S.; et al. Tuning the Li^+ solvation structure by a "bulky coordinating" strategy enables nonflammable electrolyte for ultrahigh voltage lithium metal batteries. *ACS. Nano.* **2023**, *17*, 9586-99. DOI
47. Eshetu, G. G.; Diemant, T.; Hekmatfar, M.; et al. Impact of the electrolyte salt anion on the solid electrolyte interphase formation in sodium ion batteries. *Nano. Energy.* **2019**, *55*, 327-40. DOI
48. Luo, D.; Xu, J.; Guo, Q.; et al. Surface-dominated sodium storage towards high capacity and ultrastable anode material for sodium-ion batteries. *Adv. Funct. Mater.* **2018**, *28*, 1805371. DOI